Joule

CellPress
OPEN ACCESS

Article

Increasing the performance of an anion-exchange membrane electrolyzer operating in pure water with a nickel-based microporous layer

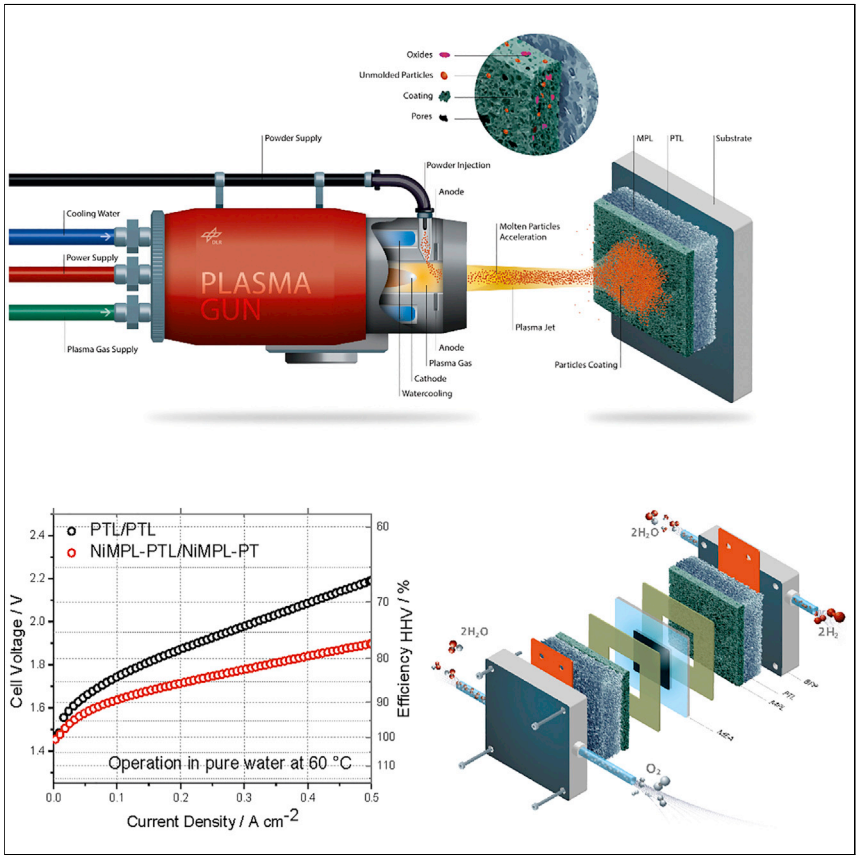

It has been technologically challenging to create an anion-exchange membrane water electrolyzer (AEMWE) that can operate efficiently without liquid electrolytes, that is, in pure water. Prior improvements in AEMWE have been limited to the development of membranes and catalysts. Here, we report an alternative solution to increase the AEMWE performance from a different perspective by developing highly conductive, macroporous layers (MPLs) as multifunctional liquid/gas-diffusion layers (LGDLs).

Fatemeh Razmjooei, Tobias Morawietz, Ehsan Taghizadeh, ..., Aldo Saul Gago, Syed Asif Ansar, Kaspar Andreas Friedrich

fatemeh.razmjooei@dlr.de

Highlights

LGDL is developed for AEMWE operated in pure water

The ohmic and mass-transfer losses were reduced significantly

The performance increased for both precious- and nonprecious-metal-based AEMWE

Razmjooei et al., Joule 5, 1776–1799
July 21, 2021
https://doi.org/10.1016/j.joule.2021.05.006

CellPress
OPEN ACCESS

Joule

Article

Increasing the performance of an anion-exchange membrane electrolyzer operating in pure water with a nickel-based microporous layer

Fatemeh Razmjooei,[1,6,*] Tobias Morawietz,[1,2,5] Ehsan Taghizadeh,[3] Efi Hadjixenophontos,[1] Lukas Mues,[4] Martina Gerle,[1] Brian D. Wood,[3] Corinna Harms,[4] Aldo Saul Gago,[1] Syed Asif Ansar,[1] and Kaspar Andreas Friedrich[1,5]

SUMMARY

Anion-exchange membrane water electrolysis (AEMWE) suffers from low performance compared with mainstream electrolysis techniques. Attempts at improvement have been confined to the development of membranes and electrodes. Here, in the quest of increasing the performance of AEMWE, a well-designed liquid/gas-diffusion layer (LGDL), termed as NiMPL-PTL, was developed by introducing nickel-based microporous layers (MPLs) on the top of a porous transport layer (PTL). The low tortuosity of this NiMPL-PTL reduced the capillary pressure and bubble point, which led to lower transport polarization. Moreover, the NiMPL-PTL decreased the interfacial contact resistance (ICR) by increasing the contact area between the PTL and the membrane electrode assembly (MEA). NiMPL-PTL, therefore, led to measurable performance improvements in the AEMWE operated in pure water: 290 mV lower voltage at 0.5 A cm^{-1} for AEMWE with MEA having precious- or non-precious-metal-based catalyst, compared with similar cells but without NiMPL-PTL.

Context & scale

Electrolytic hydrogen is advocated to decarbonize industry and transport and for energy storage. Alkaline water electrolysis (AWE) and proton-exchange membrane water electrolysis (PEMWE) are the primary industrially practiced electrolysis technologies. However, AWE suffers from low-rate production, limited transient flexibility, and a bulky design, although it uses no scarce materials. PEMWE overcomes the mentioned challenges of AWE, but it is costly. Anion-exchange membrane water electrolysis (AEMWE) can merge the low-cost materials of AWE with the compact design and transient capability of PEMWE. Operation of an AEMWE process with pure water is challenging, but it is a necessary breakthrough step for ultimately applying AEMWE in industrial processes. In this work, an approach for increasing performance in the AEMWE process with pure water is suggested through introducing a backing layer on a porous transport layer (PTL).

INTRODUCTION

Green hydrogen, i.e., hydrogen produced by water electrolysis fed with renewable energy sources, can provide a zero-carbon chemical feedstock and energy carrier for industry, mobility, and grid-scale storage.[1,2] Among water-electrolyzer technologies, alkaline water electrolysis (AWE) is the most established, whereas proton-exchange membrane water electrolysis (PEMWE) is more efficient for the same hydrogen-production capacity and it produces a higher gas purity.[3–15] PEMWE owes these advantages to its dense cation-exchange membrane and the high kinetic activity of catalysts in acidic environments. The membrane allows a more compact stack design for PEMWE compared with AWE (enabling high-pressure operation), and it requires only water as the feed. However, PEMWE has some disadvantages, including a higher capital cost for the necessary precious-metal-based catalysts[16,17] and also for the cell components, which must be made of high-cost noble-metal-coated titanium.[18–22] These expensive metals are the only materials that can bear the highly acidic and corrosive environment of PEMWE originating from the acidic nature of the perfluorinated polymeric membrane. Because of these challenges, AWE is still the most widely deployed technology for large-scale hydrogen production; the technology can be conducted with nonprecious-metal-based catalysts and requires less expensive components for construction.[9,20,23–25] However, the need

for a separate KOH circuit makes the system more complex and operationally somewhat cumbersome.

In order to combine the advantages of both systems, a considerable amount of time and effort have been devoted over the last decade on the development of the technology known as anion-exchange membrane water electrolysis (AEMWE). In this approach, the membrane conducts anions instead of cations,[26–31] thus, no KOH solution is required. Water electrolysis occurs in the catalyst layers of the membrane electrode assembly (MEA), which contains an anion-exchange membrane (AEM) and an ionomer with high ionic conductivity.[26–33] The AEMWE uses a thinner membrane, which leads to a more compact design with lower ohmic losses. In addition, because of the presence of a polymer electrolyte membrane, AEMWE also exhibits simpler gas separation and an improved operational safety than for AWE with a porous diaphragm.[26–33] All these advantages make AEMWE more efficient with higher power density than AWE. Moreover, the alkaline nature of the membrane permits the use of non-precious-transition-metal electrocatalysts and inexpensive cell components.[26–35] In summary, AEMWE aims to merge the low cost of AWE with the high power of PEMWE.[26–36]

Generally speaking, the electrochemical water-splitting performance of AEMWE is still much lower than that of PEMWE.[37] This is due to two primary reasons. First, the electrolyte membrane in PEMWE has higher ionic conductivity than the one in AEMWE.[38,39] Second, not only the oxygen evolution reaction (OER) at the anode side is a sluggish reaction in AEMWE, which is true in PEMWE as well, but also hydrogen evolution reaction (HER) at the cathode side becomes sluggish in neutral and alkaline conditions.[40] Therefore, (see Figure S1), the major voltage loss of a typical AEMWE is due to (1) the ohmic loss caused mainly by the ion conduction through the membrane and (2) the activation loss consisting of both anode and cathode overpotential.[14] Thus, the development focus in numerous studies, so far, has been either on improving the conductivity of AEM or on investigating highly active catalysts.[29,32,33] However, it is worth mentioning that the ohmic loss is not confined to the ionic resistance of the membrane, but it is also a function of the electrical resistance at the interface between the porous transport layer (PTL) as a multifunctional liquid/gas-diffusion layer (LGDL) and MEA (Figure S1A).[41] In particular, PTLs have a large effect on the electrolyzer performance.[42] PTLs are able to reduce ohmic and concentration overpotentials, which are the dominant factors for the total cell voltage.[22] PTLs need to be optimized to deliver their versatile characteristics.[43–50] The main functions of PTL principally consist of (1) providing an electrical connection between MEA and bipolar plates, (2) conveying the fluid by capillary action from the reservoir through microchannels to the reaction sites, (3) allowing diffusion of gaseous oxygen and hydrogen to the flow channel in a direction opposite to the water flow, and (4) maintaining uniform temperature distribution and efficient heat transport within the MEA.[22,43] The multifunctional PTLs can be developed and optimized by taking these versatile roles into consideration. Therefore, designing efficient multifunctional PTLs might potentially lead to AEMWE cell designs with improved performance.

It has been reported that the interface between the PTL and the MEA plays a very important role in the performance of PEMWE.[21,22,41] A conductive backing layer, or microporous layer (MPL), with optimal designs of thickness, porosity, and pore size/shape can yield low interfacial contact resistance (ICR), which decreases the ohmic resistance.[21,22] Furthermore, MPLs with low capillary pressure mitigate the mass-transfer issues at high current densities and increase the overall efficiency of

[1]Institute of Engineering Thermodynamics, German Aerospace Center, Pfaffenwaldring 38-40, 70569 Stuttgart, Germany

[2]Dep. of Basic Science, University of Applied Sciences Esslingen, Kanalstrasse 33, 73728 Esslingen, Germany

[3]School of Chemical, Biological and Environmental Engineering, Oregon State University, 116 Johnson Hall, Corvallis, OR 97331, USA

[4]Institute of Engineering Thermodynamics, German Aerospace Center, Carl-von-Ossietzky-Str. 15, 26129 Oldenburg, Germany

[5]University of Stuttgart, Institute of Building Energetics, Thermal Engineering and Energy Storage (IGTE), Pfaffenwaldring 31, 70569 Stuttgart, Germany

[6]Lead contact

*Correspondence: fatemeh.razmjooei@dlr.de

https://doi.org/10.1016/j.joule.2021.05.006

electrolyzer. Up to the present, research efforts have been primarily focused on the development of conductive membranes/ionomers and active catalysts to improve the overall performance of the AEMWE.[27–33,51,52] However, there is a lack of information on optimization of other cell components of AEMWE in order to improve its performance. In particular, designing a novel multifunctional conductive MPL mounted on the PTL is one area where further improvement of AEMWE performance might be found.

In this work, we developed a novel nickel-based backing layer on PTL (NiMPL-PTL) for AEMWE, which radically improves the cell performance under operation with pure water. This NiMPL-PTL represents a key component with multifunctionality, improved liquid/gas transport, and an improved electrical connection between the PTL and the MEA. Therefore, a significant mitigation of mass-transport issues at high current densities and improvement of ICR are achieved by implementing NiMPL-PTL as the multifunctional PTL in the AEMWE operated in pure water. To the best of our knowledge, there has not been a previous report claiming a porous layer at the interphase between the electrodes and the PTL that can increase so significantly the cell performance of the AEMWE operating with pure water.

RESULTS AND DISCUSSION

Fabrication and physical properties of NiMPL-PTL

Porous nickel-based MPLs were produced by spraying globular gas-atomized Ni-based powders by air-plasma spraying (APS) on the top of 4 cm^2 metallic PTLs. The feedstocks were Ni-carbon (Ni/C) powders with an average grain size of 10–15 μm (Figure S2A). The presence of Ni and C in the feedstock powder is confirmed by X-ray diffraction (XRD) analysis (Figure S2C). The schematic illustration of the multifunctional NiMPL-PTL fabrication using the direct current (DC) plasma-spray method is depicted in Figure 1. A Triplex-Pro210 plasma gun is used for APS where Ar is the primary plasma-forming gas and H_2 and/or He are used as secondary gases. As can be seen in Figures 1A and 1B, a Ni-based alloy was deposited on the top of PTL by using the APS process (see experimental procedures). The NiMPL coated on the top of the PTL is designated as NiMPL-PTL and the bare substrate as PTL. The bare PTL and NiMPL-PTL are implemented in the AEMWE cell assembly. As can be seen in Figure 1C, the NiMPL-PTLs are implemented as the multifunctional PTLs in the AEMWE cell in order to decrease the interfacial-contact resistance and mitigate the mass-transfer issues and subsequently improve the overall cell performance.

Once the PTL was coated with Ni-based layers, the resulting structure was characterized by XRD to determine the induced changes in the crystallographic structure of the material.

Figure 2A shows the XRD patterns of the PTL with and without Ni-based MPL. One can observe that the uncoated PTL as the substrate with the main peaks of the $Co_{0.8}$ $Cr_{0.8}$ $Fe_{0.8}$ $Mn_{0.8}$ $Ni_{0.8}$ (PDF#. 00-065-0528) has no effect on the coating peaks. This suggests that the coating is thick enough, which makes the PTL opaque.[53] For the NiMPL-PTL, the three intense diffraction peaks between 40 and 80° can be well indexed to the planes of (111), (200), and (220) of nickel (PDF#. 00-004-0850) and the small typical peak at the lowest angle is attributed to the (002) plane of graphene (PDF#. 01-082-9929) suggesting the full coverage of PTL substrate with Ni-based layers. Surface images from scanning electron microscopy (SEM) imaging in Figures 2A′ and 2A″ clearly show that the PTL substrate is fully covered by the NiMPL during

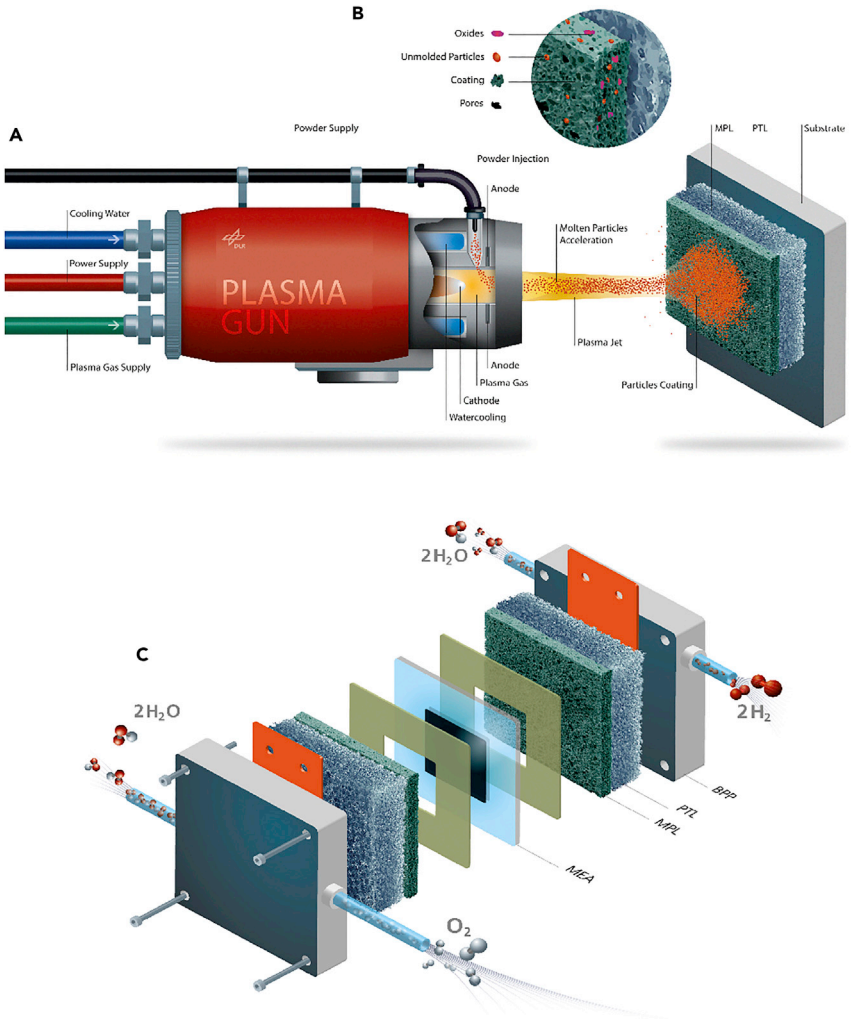

Figure 1. NiMPL fabrication and AEMWE cell assembly

(A) Schematic illustration of APS coating of NiMPL on PTL.

(B) Schematic structure of a thermal sprayed coating.

(C) Schematic of the AEMWE cell configuration with NiMPL-PTLs.

the plasma spraying, indicating the advantage of APS technique, in which large plates of PTLs with a high aspect ratio can be fully coated.[53,54] However, in the XRD pattern of NiMPL-PTL, some additional small peaks, attributed to NiO (PDF#. 00-047-1049) with significantly lower intensity than the pure Ni peak, can be observed and suggest that the surface passivation and partial Ni oxidation at high temperature during thermal-plasma spraying operated in air.

The cross-sectional SEM image of the NiMPL-PTL in Figures 2A′ and 2B show that the NiMPL drastically decreases the aperture size of the PTL, which is directly in contact with the MEA. This can lead to a larger contact area between MEA and PTL and reduction of the contact resistance in the cell, which can improve the overall AEMWE cell performance. As can be observed in Figure 2C, most of the globular particles of the Ni-based alloy were melted during the deposition, resulting in producing a very porous NiMPL coating with a thickness of ≅80 μm. This result supports the XRD observations in which the diffraction pattern of the PTL substrate has not been detected

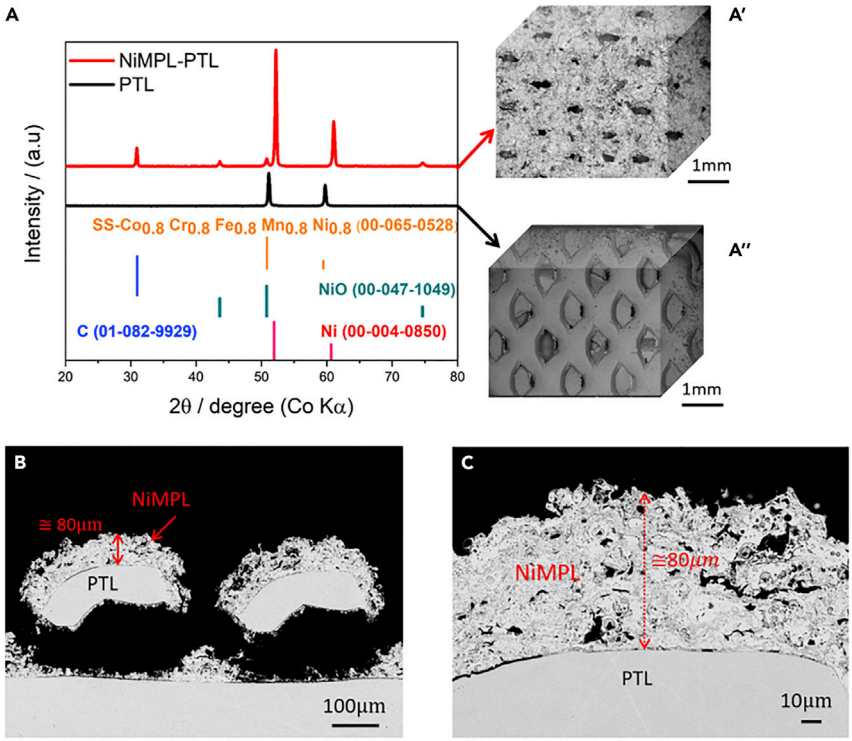

Figure 2. XRD analysis and cross-sectional SEM images of NiMPL-PTL

(A) XRD diffraction uncoated PTL and NiMPL-PTL compared with the theoretical peaks of related phases. SEM surface images of (A′) NiMPL-PTL and (A″) uncoated PTL.

(B and C) Side view SEM images of NiMPL-PTL at low and high magnification, respectively.

after coating with Ni alloy due to the appropriate depth of the NiMPL coating. As shown in Figures 2B and 2C, SEM images of NiMPL-PTL show a highly porous structure, with different pore sizes and several gaps between layers. In the APS process, pores depending on their formation mechanisms and sizes can be categorized as open pores and interlamellar flat pores.[55,56] The open pores are formed by different sources such as enclosed gases, interaction between particles and gaseous media, partial filling in the solidifying splats, and shrinking of splats during fast solidification.[57,58] However, interlamellar flat pores with convex shape, such as thin voids, are formed by splashing on impact with deposited material or voids resulting from the deformation of partially molten particles. They fill the spaces between splats, and they are usually perpendicular to the spraying direction. From the cross-section SEM images of NiMPL-PTL in Figures 2B and 2C, one can observe various pores with different shapes and sizes, which correspond to both types of open pores and interlamellar flat pores formed during the plasma spraying. Some of the pores can also be formed due to the partial oxidation of carbon to the gaseous phases.

The PTLs are responsible for distributing liquid water through the cell and providing pathways for oxygen and hydrogen gas removal. Therefore, their structure and porosity influence the behavior of gas-bubble growth and removal during the electrochemical reaction, affecting the overall cell performance. These porosities are needed to allow efficient mass transport of reactants and products without diffusion limitations.[59] Therefore, the highly porous structure of the NiMPL-PTL with a wide range of microsizes can facilitate the mass-transfer rate, which increases the overall AEMWE cell performance.

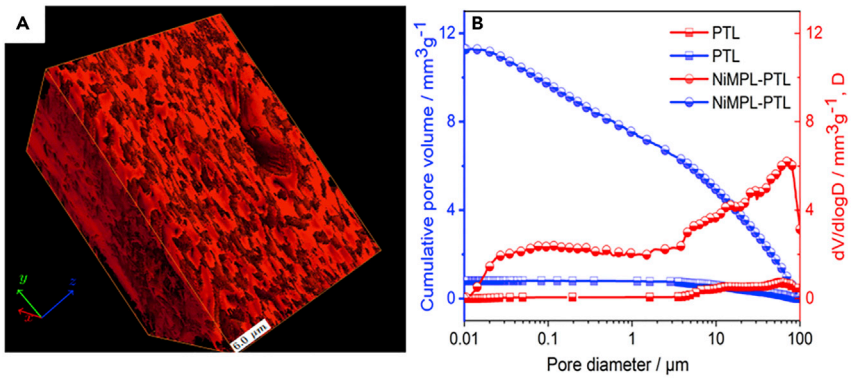

Figure 3. 3D structures and porosity of NiMPL-PTL

(A) 3D visualization of the NiMPL-PTL obtained from FIB-SEM images using Avizo software.

(B) Pore-size distributions and cumulative pore volume calculated by mercury-intrusion porosimetry (MIP) for uncoated PTL and NiMPL-PTL after cleaning.

A dual-beam focused ion beam-scanning-FEG electron microscope (FIB-SEM) is used to investigate the three-dimensional (3D) internal structures and porosity of the NiMPL-PTL. After noise reduction, segmentation, and reconstruction of the 240 SEM images obtained from FIB-SEM analysis, a 3D visualization of the NiMPL-PTL was assembled as shown in Figure 3A. The red color represents the solid phase, and the free volume displays the pore phase. As shown in Figure 3A, the final 3D image of the NiMPL-PTL features a high number of pores with different pore sizes distributed all over the sample. The porosity of the NiMPL-PTL obtained by the FIB-SEM analysis was compared with the one obtained by mercury-intrusion porosimetry (MIP) and X-ray computed tomography (μ-CT). Figure S3 presents cross-section images of the NiMPL-PTL from micro μ-CT analysis, providing optical impressions of the porosity all over the sample. Numerical data from the reconstructed scans are obtained with the analysis program CTAn. The calculated porosity in 3D space, based on a surface-rendered volume model, is 32.8%. The porosity analysis of NiMPL-PTL obtained with all three techniques (FIB-SEM, μ-CT, and MIP) reveals a porosity in the range of 30% to 40%, which is significantly larger than that of bare PTL substrate (obtained by MIP) (Figure S4). The porosimetry measurements performed by the reconstructed 3D volume, MIP, and μ-CT show good agreement among all corresponding methods. MIP measurements are used to determine the cumulative pore volume and pore-throat size distribution curves of PTL and NiMPL-PTL. Figure 3B exhibits the cumulative pore-volume and pore-size distribution curves of uncoated PTL and NiMPL-PTL. The left y axis is the cumulative pore-volume curve, which is plotted as a function of the pore diameter. The total pore volume is 11.29 mm^3g^{-1} for NiMPL-PTL, which is significantly higher than that of bare PTL with 0.85 $mm^3\ g^{-1}$. The right y axis is the logarithmic differential pore-volume distribution (dV/dlogD), which is plotted as a function of pore diameter. Compared with the uncoated PTL with no micropores, the NiMPL-PTL shows significant pores in the range from ~0.1 to 90 μm. The small pore size (ranging from 0.01 to 0.1 nm) increased after cleaning the NiMPL-PTL surface (see experimental procedures) to remove the surface oxide (Figure 3B) and porosity reaches to 54%.

To evaluate the internal elemental composition of the NiMPL-PTL, corresponding energy dispersive X-ray (EDX) mapping of the selected area in the FIB-SEM image is analyzed and shown in Figures S5A and S5B. The EDX elemental-mapping image indicates the existence of Ni (blue), C (purple), and O (yellow) in the NiMPL-PTL. As

shown in the inset of Figure S5B, the EDX line scan at the selected position indicated by the dotted arrow showed the presence of Ni with 97.1 wt % as the main element. C (2.1 wt %) and O (0.8 wt %) were also detected.

To show the improved electrical and interfacial contact behavior as a result of surface modification using the APS coating technique, we performed ICR and conductivity measurements under different compaction forces (Figures S6A and S6B).[60] The ICR decreased and the conductivity of the PTLs increased with increasing force applied by a hydraulic press. The high ICR and low conductivity at low compaction forces are due to insufficient contact pressure causing high resistance for the electric current. Therefore, with increasing force the contact area of the MPL and MEA increased. The results showed that the NiMPL coating was significantly effective on lowering ICR and the ICR of NiMPL-PTL is almost a quarter of bare PTL. The increased contact area between PTL and MEA can be attributed to the reduced aperture size of PTL induced by MPL coating, which in turn can reduce the contact resistance in the cell and consequently improve the overall AEMWE cell performance.

Effect of the NiMPL-PTL as a backing layer on the performance of the AEMWE cell with both precious- and nonprecious-metal-based MEAs

As schematized in Figures 4A, 4B, S7A, and S7B, the NiMPL-PTL and bare PTL were implemented in the AEMWE cell to investigate their effects on cell performance. Four different cells with various configurations were assembled placing the precious-metal (iridium and platinum-carbon) (Ir & Pt/C)-based MEAs (see the experimental procedures section) between two uncoated PTLs for the anode and cathode sides (PTL/PTL; Figure 4A), uncoated PTL for the cathode side and NiMPL-PTL for the anode side (PTL/NiMPL-PTL; Figure S7A), NiMPL-PTL for the cathode side and uncoated PTL for the anode side (NiMPL-PTL/PTL; Figure S7B), two NiMPL-PTLs for both anode and cathode sides (NiMPL-PTL/NiMPL-PTL; (Figure 4B). Figures 4C and S7C show the polarization curves of AEMWE cells with the four different cell configurations using precious-metal-based MEAs, operated at 60°C and atmospheric pressure in pure water. The PTL/PTL cell with precious-metal-based MEAs delivered the highest cell voltage with 2.19 V at a current density of 0.5 A cm^{-2}. However, the NiMPL-PTL/NiMPL-PTL cell with precious-metal-based MEAs delivered the lowest cell potential of 1.90 V at the same current density. Thus, an improvement of ca. 290 mV for the cell design of NiMPL-PTL/NiMPL-PTL at 0.5 A cm^{-2} compared with that of the cell with the uncoated PTLs at both sides was attained. Other cell configurations, such as the one with the NiMPL-PTLs at the anode and uncoated PTLs at the cathode for precious-metal-based MEAs, delivered a cell potential of 2.04 V at 0.5 A cm^{-2}. Changing the PTLs between anode and cathode did not improve the cell potential (2.0 V at 0.5 A cm^{-2}). The performance of these two latter cells is higher than that of the cell with the uncoated PTLs but lower than that of the cell with the NiMPL-PTLs at both anode and cathode sides. This result shows that the introduction of the NiMPL-PTLs into the cell is successfully lowering the voltage at a given current density, which can be due to the possibility that the NiMPL-PTL might provide desirable interfacial contacts with the catalyst layers of the MEAs. For comparison, one precious-metal-based MEA cell is also assembled by using a Ni mesh as PTLs at both the anode and cathode sides and tested under the same conditions. The Ni mesh/Ni mesh cell delivered higher cell potential (2.1 V) than the NiMPL-PTL/NiMPL-PTL cell. These results indicated that the NiMPL-PTL as LGDLs in AEMWE is not only much more efficient than uncoated PTL but also more efficient than the commercial Ni mesh under the current test conditions. As can be seen in Figures 4C and S7C, the AEMWE efficiency increases when the NiMPL-PTL is used in the

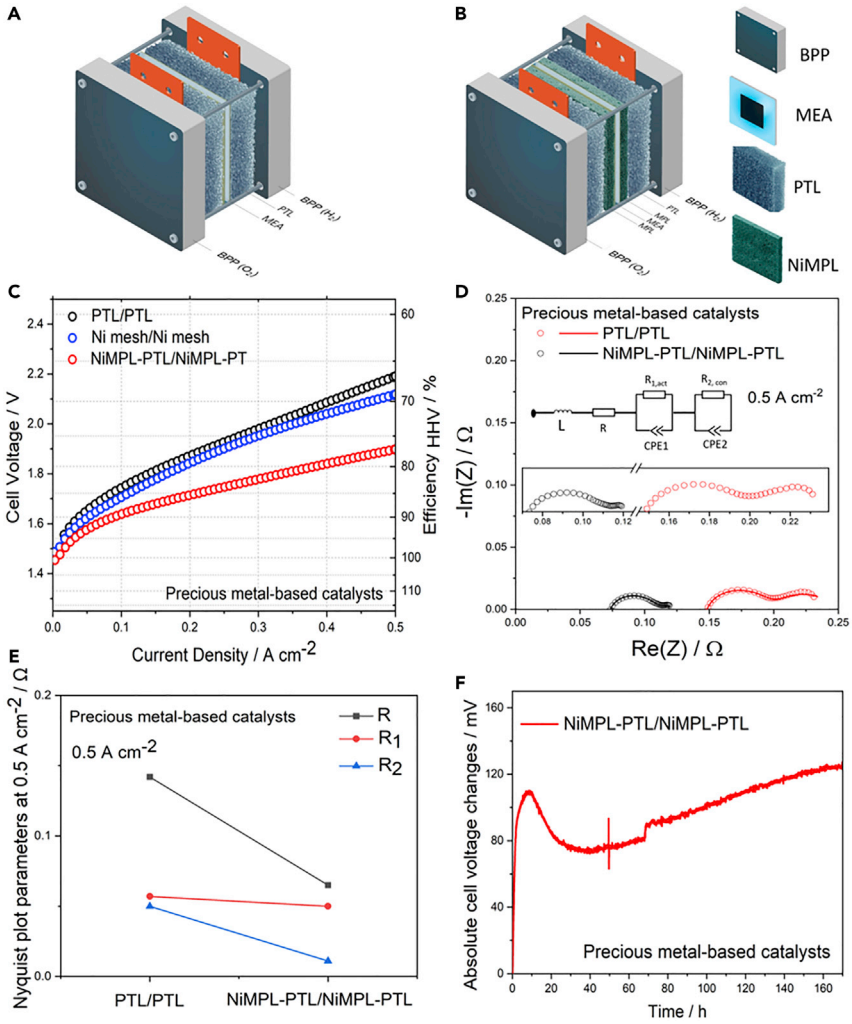

Figure 4. Impact of NiMPL-PTL on the performance of an AEMWE cell with precious-metal-based MEAs (Ir & Pt/C)

(A and B) Schematic illustration of two different AEMWE cells: (A) bare PTLs and (B) NiMPL-PTLs at both cathodic and anodic sides.

(C) Electrochemical characterization of the AEMWE with different cell configurations in pure water at 60°C (C) polarization curves for precious-metal-based MEAs (Ir & Pt/C) with different cell configurations: PTL/PTL, NiMPL-PTL/NiMPL-PTL, and a cell with commercial Ni meshes as PTLs has been tested for comparison termed Ni mesh/Ni mesh.

(D) Nyquist plots from the electrochemical impedance spectroscopy (EIS) measurements for precious-metal-based MEAs with different configurations: PTL/PTL, NiMPL-PTL/NiMPL-PTL cells at 0.5 A cm^{-2} (from 50 kHz to 100 mHz); the magnified Nyquist plots of NiMPL-PTL/ NiMPL-PTL and the equivalent circuit are shown in the inset.

(E) Nyquist plot parameters obtained from (D).

(F) Absolute voltage changes during chronoamperometric measurement at constant current density of 0.5 A cm^{-2} for the NiMPL-PTL/NiMPL-PTL cell with precious-metal-based MEA at 60°C in pure water.

cell and the highest value was obtained when the NiMPL-PTL was used at both cathode and anode sides. The efficiency increases from 66%$_{HHV}$ for the PTL/PTL cell to 77%$_{HHV}$ for the NiMPL-PTL/NiMPL-PTL cell. In other words, a 17% increment in the efficiency was observed at 0.5 A cm^{-2} for the NiMPL-PTL/NiMPL-PTL cell compared with the PTL/PTL cell. This efficiency improvement, on a system level, can have a direct, significant impact on the operational expenditure.

The NiMPL-PTL can efficiently remove gas bubbles formed at the electrode surface due to its high porosity with a broad range of microsizes. It can also decrease the contact resistance given that it increases the contact area between PTL and MEA by providing more surface through reducing the aperture size of the PTL. These can reduce the mass-transport losses and decrease the contact resistance with the MEA. As a result, significant mitigation of mass-transport issues at high current densities and improvement of the ICR are achieved by implementing the NiMPL-PTL as MPL/PTL in the AEMWE operated in pure water. Therefore, the high porosity and lower ICR enable the NiMPL-PTL/NiMPL-PTL cell to operate at higher current densities while maintaining a low operating voltage.

The positive effect of the MPL in the AEMWE was also confirmed by electrochemical impedance spectroscopy (EIS) analysis, which was systematically recorded during *in situ* full-cell testing. To analyze the EIS plots, a fitting procedure was performed with an equivalent electric circuit model. The model was chosen on the basis of the physical processes and their interactions in our system, which include ohmic, activation, and mass-transfer resistances. EIS was applied to identify the ohmic, activation, and mass-transfer losses. Figure 4D shows the analysis and comparison of the Nyquist plots with their model fits for the cells with PTL/PTL and NiMPL-PTL/NiMPL-PTL at a constant current density of 0.5 A cm^{-2}. The magnified Nyquist plots of NiMPL-PTL/NiMPL-PTL are shown in inset of Figure 4D. The effect of each loss is present in a proposed equivalent circuit model shown in the inset of Figure 4D. In the test performed with precious-metal-based catalysts the equivalent circuit includes two resistor-constant phase element (CPE) pairs from high- to low-frequency range as two semicircle loops are observed in the Nyquist plots from Figure 4D. The equivalent circuit consists of an ohmic resistance (R) in series with two circuits, each comprising a resistance (R_1, activation resistance, and R_2, concentration resistance) and a CPE1 and CPE2 in parallel to each other. The inductor (L) in series with the R represents possible inductive parts of cables and other components. The R or high-frequency resistance (HFR), which appears as the intercepts of the Nyquist plot with the x axis at high frequency (left side of the Nyquist plot), represents the internal ohmic resistance of the cell.[41] The R refers to the resistance caused by the current flow through the cell. The R is expressed as the sum of the contributions from membrane, electrodes, PTLs, bipolar plates, and contact resistances.[61] The middle section of the equivalent circuit model describes the activation loss. The activation loss (R_1)is due to the kinetics of OER and HER at the anode and cathode, respectively. It is noticeable as a semicircle at high- and middle-frequency ranges.[62] The CPE is related to the double-layer capacitance for both HER at the cathode and OER at the anode side. Given that only one semicircle from high to middle frequency has been observed, the anode and the cathode charge-transfer resistances and their CPEs are not separated and are considered to be one. R_2 represents the mass-transport limitation and resistance, which is noticeable as a small semicircle at low frequencies. Furthermore, in the case of electrochemical gas-evolving systems such as electrolyzers, the formation of bubbles can affect each of these processes. Operation of electrolyzers can lead to the accumulation of dissolved gases that eventually reach a concentration above the supersaturation threshold for bubble formation.[14] As a consequence, PTL with appropriate pore-size distributions are needed to allow the passage of a two-phase liquid/gas flow and efficient bubble removal, consequently improving the cell performance. The bubble formation can influence the efficiency of water electrolysis and have distinct effects in each of the overpotential contributions, which is also discussed below.

EIS data are analyzed by fitting to an equivalent electrical circuit model. The values of the fitted equivalent circuit model are given in Figure 4E for plots for PTL/PTL and NiMPL-PTL/NiMPL-PTL cell configurations at a constant current density of 0.5 A

cm^{-2}. It can be seen from the Nyquist plots that the semicircle shape in the range of high to middle frequencies attributed to activation resistance (R_1) slightly decreased for NiMPL-PTL/NiMPL-PTL cell (0.05 Ω) compared with that of PTL/PTL cell (0.057 Ω). This activation improvement, obtained by implementing NiMPL-PTL in the cell, can be attributed to the increased utilization of the catalyst layer due to a high contact area provided by MPLs.[21] This could be due to the fact that the pore radius of bare PTL in contact with the MEA is not appropriate enough for an optimized management of two-phase liquid/gas flow. Therefore, this can cause coalescence of bubbles and thus augmentation in the bubble size, which could cover and mask the active electrode surface, leading to the activation loss. Therefore, the implementation of NiMPL-PTL with a wide pore-size distribution in the cell might reduce the coalescence of bubbles produced at high current densities and in turn increase the utilization of the catalyst layer by improving the contact of catalytic layer. The ohmic resistances of the cells also show changes. Because the cells use the same membrane, electrodes, PTL substrates, and bipolar plates, the change in the R can be only attributed to the MPL. The effect of high-frequency tail extending toward positive imaginary parts, which is attributed to the electronics and wires on the ohmic resistance, is included. Therefore, the ohmic loss slightly deviates from the intercepts of the Nyquist plot with the x axis at high frequencies. By incorporating the NiMPL-PTL as PTLs at both the cathode and anode sides, the HFR drops to 0.065 Ω for the NiMPL-PTL/NiMPL-PTL cell compared with that of the PTL/PTL cell configuration of 0.142 Ω. The decrement in the HFR upon incorporating the NiMPL-PTLs in the cells can be attributed to the lower contact resistance of the NiMPL-PTLs compared with the bare PTL. These results are in line with the findings from ICR and polarization curves and show that the ohmic resistance drastically decreased by incorporating NiMPL-PTLs in the AEMWE cell, which can be due to the lower ICR of NiMPL-PTL compared with bare PTL. The NiMPL-PTL with appropriate pore-size distribution and low ICR can reduce the trapped-bubble concentrations between the MEA and gas-diffusion layers, which leads to an increase of the contact area and in turn can contribute to an increase the overall cell performance.

Lastly, mass-transport limitations for NiMPL-PTL/NiMPL-PTL cell with the NiMPL-PTL/PTL are negligible compared with those of the PTL/PTL cell with the bare PTLs in the low-frequency resistance (LFR) arc of the Nyquist diagram (Figure 4D). It is obvious that the mechanisms of mass-transport limitation changes with the application of the NiMPL with high porosity on the PTL. This can be caused by the lower pressure built during the cell operation due to more efficient water transport and gas removal through pore-graded MPL-coated PTL. As shown in Figure 4D, the presence of a semicircle at low frequency originating from the mass-transfer resistance can be observed for the PTL/PTL cell, whereas it became small for a NiMPL-PTL/NiMPL-PTL. The PTL/PTL cell with the bare PTL shows the LFR arc, which might indicate that the pore radius of bare PTL in contact with the MEA is not refined enough for an optimized management of two-phase liquid/gas flow. In other words, in the PTL/PTL cell, water cannot reach the MEA fast enough and the gas bubbles produced cannot be removed efficiently most likely due to lack of a proper porosity network, thus generating the back pressure. The back-pressure issue should be suppressed by water driven by capillary pressure and thus this can lead to the mass-transport issue. This developed back pressure due to formation of bubble and gas pillow between MEA and bare PTLs not only causes an increase in the mass-transfer resistance; it also results in blockage of some of the active sites and also increase of the contact resistance, which in turn increase the activation and ohmic resistance and negatively influences the PTL/PTL cell performance. This can be seen when the semicircle in the range of high to middle frequencies increases and the interception of HFR arc of PTL/PTL cell with the x axis is positively

shifted, indicating a higher resistance. This result suggests a decrease in the mass-transfer resistance by incorporating the porous NiMPL coating as an MPL and an improvement in the overall cell performance. The positive effect can be due to the high porosity, extended pore volume, and broad pore distribution at the interphase between the PTL and MEA. This is conclusive evidence for the importance of the MPL porosity, pore size, pore distribution, and liquid/gas phase transport within the anode and the cathode sides of the AEMWE cell and their crucial role in the overall cell performance. The EIS measurements are in good agreement with the polarization curves in terms of the performance. By introducing the NiMPL-PTL as PTLs in both the cathode and anode sides, the R_2 drops to 0.011 Ω for the NiMPL-PTL/NiMPL-PTL cell compared with the PTL/PTL cell configuration (0.050 Ω) (Figure 4E). These results show that the mass-transfer resistance drastically decreased by incorporating NiMPL-PTLs in the AEMWE cell, which can be due to the porosity of NiMPL-PTL, which is higher than that of bare PTL.

The AEMWE cells is also operated at higher current densities up to 2 A cm^{-2}, and the current-voltage polarization curves of the NiMPL-PTL/NiMPL-PTL and PTL/PTL cells operated in pure water at 60°C are shown in Figure S8. The NiMPL-PTL/NiMPL-PTL cell is still more efficient than the PTL/PTL cell at high current densities and shows a lower cell voltage (2.5 V) than that of PTL/PTL (3.45 V) at a current density of 2 A cm^{-2}. Most importantly, EIS was systematically carried out to analyze the behavior of PTL/PTL and NiMPL-PTL/NiMPL-PTL cells at higher current densities. As shown in Figures S9A and S9B, the presence of a semicircle at low frequency originating from the mass-transfer resistance can be observed for the PTL/PTL cell, whereas it became smaller for a NiMPL-PTL/NiMPL-PTL in the higher current densities. Therefore, this shows that mass-transport limitations are negligible for the NiMPL-PTL/NiMPL-PTL cell compared with those of the PTL/PTL cell even at higher current densities, where the gas production rate is high. This supports the notion that the mechanisms of mass-transport limitation change with applying the NiMPL with high porosity on the PTL. This can be caused by lower pressure built during cell operation due to more efficient water transport and gas removal through porous MPL-coated PTL. As can be seen in Figures S9A and S9B, the NiMPL-PTL/NiMPL-PTL cell shows smaller ohmic loss, as the intercepts of the Nyquist plot with the x axis at high frequency, in all the current densities. The decrement in the ohmic loss that results from incorporating the NiMPL-PTLs in the cells can be attributed to the lower contact resistance of NiMPL-PTLs compared with that of bare PTL. Overall, these results show that the developed NiMPL-PTL increases the cell performance and does not lose any advantage even at higher current densities. It is worth mentioning that, due to the early stage of development of the AEMWE technology in pure water, the operation at high current densities, which decreases substantially the cell-voltage efficiency, might increase the corrosion of other cell components such as the membrane and ionomer.

The short-term durability of NiMPL-PTL/NiMPL-PTL cells with precious-metal-based MEAs in pure water was evaluated under a large current density of 0.5 A cm^{-2} at 60°C for 170 h, and the absolute cell-voltage changes as a function of test time are shown in Figure 4F. The cell voltage shows a 53 mV increment over the 170 h after the first initial voltage increase during the few hours of operation, which is reported to be due to the ionomer oxidation.[63] This degradation rate even at such a high current density is lower than the currently reported AEMWEs in pure-water-operated at a lower current density of 0.2 Acm^{-2}.[63] The durability of AEMWEs mostly depends on the stability of membrane and ionomer.[28,63] However, the currently available commercial AEMs and ionomers used in AEMWE are still at an

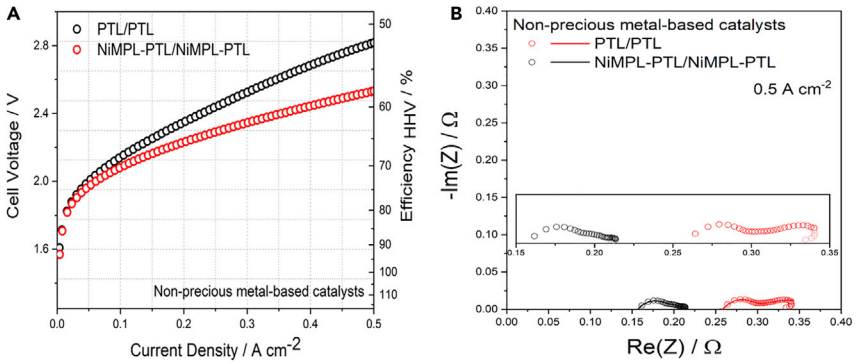

Figure 5. Effect of NiMPL-PTL on the performance of AEMWE cell with nonprecious-metal-based MEA

Electrochemical characterization of the AEMWE based on the cell configuration with nonprecious-metal-based catalysts. Different PTLs (PTL/PTL and NiMPL-PTL/NiMPL-PTL) in pure water at 60°C. Acta 4030 was used as a cathode and Acta 3030 as an anode.

(A) Polarization curves for nonprecious-metal-based MEAs with different configurations: PTL/PTL and NiMPL-PTL/NiMPL-PTL.

(B) Nyquist plots from the EIS measurements for nonprecious-metal-based MEAs with different configurations: PTL/PTL and NiMPL-PTL/NiMPL-PTL at 0.5 A cm^{-2} (from 50 kHz to 100 mHz). Magnified Nyquist plots of NiMPL-PTL/NiMPL-PTL are shown in inset.

early stage of development and are not yet competitive with their counterparts—the cationic-exchange membrane and the proton conductive ionomer in PEMWE. The slight increase in the cell voltage from the durability test can be due to the loss of ion-exchange capacity (IEC) in the membrane or partial ionomer oxidation at high current density.[28,63] As shown in Figure S10A, the XRD pattern of NiMPL-PTL after the durability test remains the same as before the durability test with slightly increased NiO peak intensities. As can be seen in Figures S10B and S10C, the EDX analysis of NiMPL-PTL exhibits the increase of light blue color in the EDX images in the oxygen mapping compared with that of NiMPL-PTL before the test. The increase of O content can be due to the typical oxidizing environment of an electrolyzer. However, the MPL structure is quite well retained after the durability test.

The durability test for PTL/PTL cells has been also performed at 0.5 A cm^{-2} for 120 h. As shown in Figure S11, the AEMWE cell exhibits an absolute cell-voltage change of almost 210 mV over 120 h of continuous chronopotentiometric operation at a constant current density of 0.5 A cm^{-2}. The test was stopped at this time as the cell voltage was already too high and, thus, the efficiency was very low. The high degradation of the PTL/PTL cell can be attributed to loss of IEC in the membrane and membrane degradation. Due to inappropriate gas removal caused by low porosity of bare PTLs, the gaseous phase contents in the vicinity of the electrode will rise, and given that the thermal conductivity of gaseous phase (e.g., oxygen gas at the anodic side) is significantly less than that of liquid water, a large increase in thermal resistance can be created and will lead to the formation of hot spots, which can accelerate the degradation of the membrane.[64,65]

Figure 5A presents polarization curves for two cells, PTL/PTL and NiMPL-PTL/NiMPL-PTL, using nonprecious-metal-based MEAs (commercial Acta 4030 at the cathode and Acta 3030 at the anode). The same trend exhibited by precious-metal-based MEAs has been observed for nonprecious-metal-based MEAs when bare PTLs are replaced by NiMPL-PTL. The NiMPL-PTL/NiMPL-PTL cell using nonprecious-metal-based MEAs delivered lower cell potential 2.53 V and higher

efficiency 58% at 0.5 A cm^{-2} than the PTL/PTL cell with a potential of 2.82 V and efficiency of 52 %, respectively.

Figure 5B shows the analysis and comparison of the Nyquist plots for two cells of PTL/PTL and NiMPL-PTL/NiMPL-PTL with nonprecious-metal-based MEAs at a constant current density of 0.5 A cm^{-2}. In the test performed with nonprecious-metal-based catalysts, the equivalent circuit includes three resistor-CPE pairs from high- to low-frequency range as three semicircle loops are observed in the Nyquist plots from Figure 5B. The two semicircles in the range of high to middle frequency represent activation loss, which is due to the kinetics of OER and HER at the anode and cathode. The presence of two semicircles at high to middle frequency can be attributed to the presence of OER and HER, which are both kinetically sluggish in alkaline and neutral condition specifically with nonprecious-metal-based catalysts. Expensive platinum-based catalysts are still the most active catalysts in alkaline conditions.[40,66] This behavior can be realized when, in a recent report on AEMWE cells operated in pure water, the cell performance improved and reached the performance of precious-metal-based MEA at 0.5 A cm^{-2} when NiMo cathode is replaced with Pt/C.[63] It is also reported for AEMWE operated in 0.1M KOH that the cell performance improved and the activation loss decreased drastically when NiMo/C is replaced by Pt/C with a precious-metal anode present in both cases.[67] This can be due to the fact that the first step during the HER in alkaline and neutral condition involve water dissociation, which is thought to be the reason for slower HER in base than in acid media.[68] In our work, we found that the first semicircle, which can be attributed to HER, is larger than the one for OER for nonprecious-metal-based MEA operated in pure water, suggesting that the cathode is the dominant obstacle in charge-transfer resistance in this particular system. A further investigation of catalysts' material properties and their impedance signatures will require systematic investigations going beyond the scope of this manuscript. Therefore, the sum up two resistance obtained from Nyquist plot of nonprecious-metal-based catalysts in high to middle frequency is considered to be activation loss. The same trend as the precious-metal-based MEAs has also been observed for nonprecious-metal-based MEAs when bare PTLs are replaced by NiMPL-PTL for all the ohmic, activation, and mass-transfer losses. The effect of the high-frequency tail extending toward positive imaginary parts, which is attributed to the electronics and wires on the ohmic resistance, is included. As can be seen in Figures 5B and S12, the R decreases for NiMPL-PTL/NiMPL-PTL cell (0.12 Ω) compared with that of the PTL/PTL cell (0.21 Ω) with nonprecious-metal-based MEAs, which can be attributed to the lower contact resistance of NiMPL-PTLs compared with that of bare PTL. The higher ohmic resistance for nonprecious-metal-based MEA compared with precious-metal-based MEA can be attributed to their lower electronic conductivity. The same trend has been observed for the mass-transport resistance, which is noticeable as a small semicircle at low frequencies. As shown in Figure 5B, the presence of a semicircle at low frequency originating from the mass-transfer resistance can be observed for the PTL/PTL cell with nonprecious-metal-based catalyst MEAs, whereas it became smaller for its counterpart NiMPL-PTL/NiMPL-PTL cell, indicating a lower mass-transfer resistance (0.018 Ω) than that of the PTL/PTL cell (0.034 Ω). This can be attributed to the presence of MPLs which can facilitate the water transport and gas removal during cell operation. It can be seen from the Nyquist plots that the semicircle shape in the range of high to middle frequencies attributed to activation resistance (R_1+R_2) decreased for NiMPL-PTL/NiMPL-PTL cells (0.087 Ω) compared with that of PTL/PTL cell (0.12 Ω), which can be attributed to the increased utilization of the catalyst layer due to a high contact area provided by MPLs.[21]

It is not easy to compare our AEMWE performance with literatures because no data for Sustainion membranes/ionomers or Acta 4030 cathode operating in pure water. Using MEA with precious-metal-based catalysts and with the ionomer and membrane from Tokuyama operated in pure water, Leng et al. reported a performance of 1.90 V at 0.5 A cm^{-2}, although with a low durability.[32] This performance is comparable to our results with precious-metal-based MEA and MPL modification. In another study on AEM, using precious metal at the cathode and Acta 3030 as an anode (the same non-precious metal used in our work), a high cell potential of 2.4 V under 0.2 A cm^{-2} with the Tokuyama membrane and ionomers operated in pure water was reported.[69] Recently, very high performance of 2.7 A cm^{-2} at 1.8 V (~1.55 V at 0.5 A cm^{-2}) was reported for AEM with precious metal as cathode and NiFe catalyst as anode and with a novel HTMA-DAPP membrane/ionomer. However, the durability of the MEA was tested under low current density of 0.2 A cm^{-2} and remained a challenge.[63] Hence, as AEMWE is still in the early stages of development, all the components (membrane, ionomer, catalysts, LGDL, cell design, etc.) need to be optimized together to deliver a high-performance AEMWE in pure water in terms of both initial performance and long-term durability. Today, it is not feasible to exactly rank or compare the available reported AEMWEs because any experimental ranking would be confined to certain materials or testing conditions. It should also be noted that the performance of AEMWE in our work has been achieved without any optimization of catalyst and membrane/ionomer for pure water, and the available commercial catalysts and membrane/ionomer were used. We focus here on the comparison of PTL and the beneficial effect of MPLs. We are convinced that the performance of the AEMWE can be further improved by combination of the NiMPL-PTL with the optimized ionomer, membrane, and catalysts, if developed to operate in pure water.

Numerical simulations

An explanation of the mass-transport behavior of the MPL might be realized through further understanding of the morphology of its porous structure. Characteristic for the structure is a bimodal size distribution, which combines the benefits of both pore sizes. For fuel-gas-diffusion layers, the pore-size distribution was found to be more important than total porosity for obtaining high performance.[70] The most effective structure appears to be a combination of small pores with a high contact area and bigger pores with a low tortuosity for effective high mass transport.[71] To describe the material properties in more detail, a series of simulations were carried out, including calculations of the capillary-pressure curves and bubble points. Capillary pressure versus saturation curves for drainage and imbibition were simulated using the μ-CT-measured structure to investigate the mass-transport behavior of NiMPL-PTL MPL. These parameters are strongly influenced by the pore properties of the MPL. The result of the simulated drainage and imbibition curves of the NiMPL-PTL are displayed in Figure 6A. Water saturation of NiMPL-PTL at different capillary pressures is simulated, and accordingly the air imbibition into a water-filled NiMPL-PTL and drainage from air-saturated NiMPL-PTL are obtained. In the simulated curves the typical hysteresis between drainage and imbibition is visible.[72] A capillary pressure of 56.8 kPa was calculated for a full-wetting phase saturation. A fast drop in capillary pressure is recognized for imbibition and drainage experiments, which suggests that, even at a low saturation of gas, the pressure needed for pressing the water out of the porous structure reduces fast and the flow is assured. The liquid-water permeability is enhanced with bigger pores from the PTL underneath whereas the small pores of the MPL decrease gas saturation, depending on the material properties during operation.[73] The small pores will help to exchange the wetting phase, when the large pores are saturated.

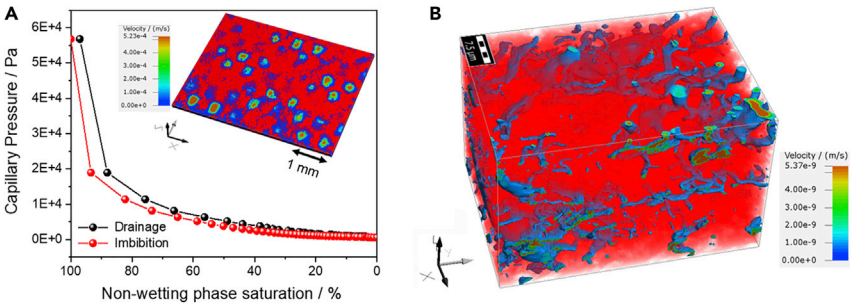

Figure 6. Mass-transport behavior of the NiMPL-PTL

(A and B) Saturation and flow simulation of NiMPL at different scales. (A) capillary pressure versus saturation curves for drainage and imbibition of water and simulated flow of water through the MPL obtained from μ-CT and (B) simulated water flow through the FIB-SEM-measured structure.

In addition to the capillary-pressure curves, the flow of water through the material was simulated to visualize the connected paths through the material. The results of the water flow of the μ-CT measured MPL is shown in Figure 6A next to the capillary-pressure curves (inset). The flow through the FIB-SEM-measured structure is visible in Figure 6B. It is visible that even the small pores can be involved in the flow through the structure. The local speed of the flux was determined. As a result, a flow of 2.38×10^{-5} m/s through the μ-CT structure at an assumed pressure difference of 0.02 Pa was simulated. The average flow velocity at 0.02 Pa was 9.48×10^{-10} m/s in the x direction, 9.83×10^{-10} m/s in the y direction, and 9.01×10^{-11} m/s in the z direction for the FIB-SEM structure. The higher flow rate through the whole μ-CT structure is determined by the bigger pores. Still, an additional flow through the smaller pores by the wetting phase is advantageous for a high total flow when the bigger pores are saturated. Based on the capillary-pressure curves, the relative gas diffusion and gas permeability were simulated. Simulation results of the relative gas diffusivity and permeability were obtained for the μ-CT and the FIB-SEM structures to consider the different resolution of these techniques and the resulting structures. Relative gas permeability gives an impression of the flow of gas, which is hindered due to the presence of water. The results of the gas saturation and gas permeability simulation of the NiMPL-PTL at a gas saturation level of 0.5 is shown in Figures S13A and S13B. In accordance with the capillary-pressure curves the permeability changes at different saturation levels. It is visible in the results of the μ-CT structure that the small pores are mostly responsible for the wetting-phase transport and the bigger pores are responsible for the nonwetting transport (Figures S14A–S14H). The relative diffusivity at different saturation levels of the μ-CT structure can be found in Figures S15A–S15D. The results of the relative diffusivity and the relative permeability at different saturation levels of the FIB-SEM-measured structure can be found in Figures S16A–S16I. In addition, the values are given in Table S1. It is visible in the results of the μ-CT structure that the small pores are mostly responsible for the wetting-phase transport and the bigger pores are responsible for the nonwetting phase transport. This fact shows the superior properties of this bimodal structure compared with standard PTLs. Still a certain fraction of gas is needed to enable the diffusion of gas through the small pores (Figure S17). The void space in the porous medium is assumed to be filled with the different phases. Connected channels are mainly responsible for the nonwetting flow and the rim of the pores is involved in the wetting-phase exchange. The big pores might accelerate the gas transport and less gas accumulates near the catalyst layer MPL interface, similar to the modification of commercial PTLs reported by Lee et al.,[74] thus, the water transport also is improved. Another explanation for the improved performance is

that the favored nucleation sites are outside of the NiMPL-PTL due to a diffusion flux without nucleation inside the small pores.[75]

A measure of a short travel distance for water and produced gas is the tortuosity.[76] For receiving the geometric tortuosity, Laplace diffusivity simulations or bulk diffusion were conducted on both structures. The (geometric) tortuosity τ in the z direction of the NiMPL-PTL was calculated to be 1.3. The tortuosity after testing was simulated to be 1.22 and is thus in the same range. A low tortuosity will result in a less hindered flow (lower resistance to the flow direction) of the media through the structure. For fiber-based PTLs with different fiber diameters a tortuosity between 1.2 and 1.6 with smaller fiber diameters resulting in a higher tortuosity was calculated.[77] The calculated tortuosity of the measured μ-CT structure is in the range of fiber-based PTLs, which represents a reasonable value. Comparable MPLs for water electrolysis resulted in a tortuosity of 1.5 to 1.9.[77] In addition, the tortuosity for the FIB-SEM NiMPL structure which represents the microporous contact to the MEA was calculated to be 2.31, 3.21, and 6.13 in x, y, and z directions, respectively. This part improves mainly the utilization of the catalyst layer due to a high contact area.[77] The pore size and pore properties were analyzed, and it was seen that only a negligible number of the pores were closed. Calculations with GeoDict for the μ-CT-measured structure resulted in closed porosity of only 0.52% (Figures S18A–18C). The bubble-point pressure, which is directly linked to the pore-size distribution, was simulated to be 673 Pa for the μ-CT structure. This gives an indication of the pressure required for pushing the water out of the porous structure. As can be seen in Figures S19A–S19C, after operation for 170 h a comparable amount (0.37%) of closed pores was calculated with the μ-CT-measured structure. After operation also, a decreased bubble-point pressure of 521 Pa was simulated, taking the slightly changed pore-size distribution and pore shape into account. The water flow after operation for 170 h for NiMPL-PTL in the z direction was simulated to be 4.12×10^{-5} m/s, which is also in the range of the sample before operation. The flow visualization can be found in Figure S20.

The multiple roles of the MPL in AEMWE includes providing a platform to facilitate (1) uniform distribution of reactive water on the surface of the MEA, (2) removal of gases produced on the surface of the MEA, and (3) transport of electrons to or from the external electrical circuit. In addition to the required electrical and interfacial properties, optimal PTL experimental designs with well-tuned porosity and appropriate pore distribution and pore size will be in high demand to improve further the performance of AEMWE. To meet these fundamental requirements for multifunctional PTLs, the rapid, cost effective, and large-scale APS manufacturing technology has proven to be useful. Using APS technology multifunctional backing layers on PTLs have been fabricated by coating microporous layers of Ni-based alloy on the top of a porous transport layer, which yields low ICR as well as mitigated the mass-transfer issues, which in turn can increase the efficiency of AEMWE. Therefore, well-developed, porous APS-based MPL/PTL with optimized capillary pressure and tortuosity shows lower resistance than the uncoated PTL. A total resistance (including both ohmic and mass-transfer resistance) reduction of NiMPL-PTL compared with that of bare PTL made it possible to decrease the overall operating voltage of AEMWE with a commercial membrane approximately 290 mV at 0.5 A cm^{-2} and enhance its overall performance in operation with pure water. This study highlights effect of MPLs for AEMWE operated with pure water, which have not been explored to date.

Conclusions

Currently, all research efforts have been concentrated on improving the conductivity of membrane and activity of electrocatalysts to improve the overall performance of

AEMWE. However, there remains significant room for improvement in the performance of AEMWE through optimization of other cell components or cell design, which is neglected. Here, multifunctional PTLs were developed by introducing highly porous NiMPL by using the APS technique on the top of a porous PTL and this NiMPL-PTL is applied into a pure-water-operated AEMWE for the first time. The AEMWE cell with NiMPL-PTL shows a current density of 0.5 A cm^{-2} at a very low operating voltage of 1.90 V, which was 290 mV lower than that of AEMWE cell with the uncoated bare PTL. In order to gain a better understanding the role of NiMPL-PTL as PTLs, several physical characteristics, such as capillary pressure, bubble point, tortuosity, and ICR were correlated with the electrochemical characterizations. The porosity of NiMPL was analyzed by FIB-SEM, μ-CT, and MIP techniques. The results showed that the well-tuned NiMPL-PTL reduced the total resistances, including both ohmic and mass transfer in both precious- and nonprecious-metal-based MEAs. The high porosity with a large pore-size distribution and a low tortuosity of 1.3, which is in the range of fiber-based PTLs leads to reduction of capillary pressure, which can efficiently remove the gas bubbles formed at the MEA surface. A combination of small and big pores present in the NiMPL of this work plays an important role in an effective exchange of gases and water. This was shown by simulating the water flow through the structure, which was visualized to give an impression of the connected paths through the NiMPL. The big pores might have ensured high mass transport and resulted in a low bubble point, whereas the smaller pores might have forced bubble formation outside the NiMPL and, thus, away from the catalyst layer, enabling continuous electrochemical reactions. Moreover, the NiMPL-PTL can also decrease the contact resistance because it increased the contact area between the PTL and the MEA by providing a bigger interface by reducing the aperture size of the PTL. Therefore, the high porosity with a broad range of microsizes and lower ICR of the NiMPL-PTL can reduce the mass-transfer and ohmic resistance, respectively, which can enable the AEMWE cell to operate at higher current densities while maintaining the low operation potential. This increases both AEMWE cell performance and efficiency at 0.5 A cm^{-2} with both precious- and nonprecious-metal-based catalysts compared with the AEMWE cell with uncoated PTLs. The highlight of this work is the modification of the interphase between the PTL and the MEA by applying a backing layer on the PTL, which brings benefits in AEMWE performance with pure water. This aspect has never been recognized before, opening a research area in this technology.

EXPERIMENTAL PROCEDURES

Resource availability

Lead contact

Further information and requests for resources should be directed to and will be fulfilled by the lead contact, Fatemeh Razmjooei (fatemeh.razmjooei@dlr.de).

Materials availability

This study did not generate new unique reagents.

Data and code availability

This study did not generate or analyze datasets or code.

MPL fabrication

Porous nickel-based MPLs were produced by spraying globular gas-atomized powders of Ni/C 80:20 wt % by APS on the top of 4 cm^2 PTLs made of stainless steel. The feedstocks were a mixture of Ni-based powders with an average grain size of 10–15 μm (Figure S2), HC Starck. A triplex-Pro210 plasma gun from Oerlikon-Metco

(CH) is used for APS for which Ar is the primary plasma-forming gas and H_2 and/or He are as secondary gases. The schematic illustration of the multifunctional NiMPL-PTL fabrication using the direct current (DC) plasma-spray method is depicted in Figure 1A. As can be seen in Figure 1A, a Ni-based alloy was deposited on the top of a PTL (stainless steel por graded substrate from Melikon). Briefly, in DC plasma spraying, microparticles Ni-based alloy in the form of powder is injected through external injection nozzles into the plasma jet, where particles were accelerated and heated due to momentum and heat transfer between plasma and particles and the quasi or fully molten particles impacted the substrate surface, flattened, solidified, and consolidated to form pancake-like structure MPL coatings (Figure 1B). Multiple layers are coated to form a Ni-based alloy with an appropriate thickness. The thickness of Ni-based layer was designed to be less than 100 μm, which is an empirical value to meet the fundamental requirements of multifunctional PTLs. As the structural and mechanical properties of the APS-based deposits are highly dependent on in-flight treatment of particles and inter particle cohesion, optimizing of parameters during the thermal spraying is important. The plasma enthalpy and the torch sweep rates were 12.7 MJ kg^{-1} and 400 mm s^{-1}, respectively. Key information is summarized in Table S2. The bare PTL and NiMPL-PTL are implemented as multifunctional PTLs in the AEMWE cell assembly.

MPL characterization and numerical simulation

XRD patterns of the coating samples were acquired using an X-ray diffractometer STADI P (STOE, Germany) in the Bragg-Brentano geometry with Co-Kα and also Cu-Kα source operated at 40 kV and 30 mA. To fix samples for further analysis, such as SEM and EDX, the samples are cast into resin. The applied resin is a mixture of resin and hardener with a mass ratio of 25:3. After mixing the resin components for several minutes, the bubbles produced during mixing were forced out with the help of a vacuum pump. The coated PTLs are placed in the mold and the resin mixture is poured into the mound to cover all the samples followed by drying at ambient temperature for 8 hours. Before the physical characterization the resin samples are polished using different grinding size 46, 22, 15, 9, and 3 μm to make the surface smoother and clearer. The morphology of the polished resin samples was observed with SEM using a Zeiss Gemini Ultra plus microscope operated at an acceleration voltage of 20 kV. The chemical compositions of the samples were determined by the EDX spectrometer/detector from the Bruker company. The morphology and cross-section images of the polished samples were observed with a SEM using a Zeiss Gemini Ultra plus microscope operated at an acceleration voltage of 20 kV. The μ-CT analysis was performed with the X-ray microtomograph SkyScan 1172 (Bruker) with an acceleration voltage of 80 kV and a current of 100 μA. The MPL samples were prepared by mechanically cutting them into a piece of 4 mm × 4 mm. Scans were done with an optical resolution of 2.25 μm per pixel, 180° rotation and a rotation step of 0.25°. For reconstruction of the images, the software NRecon was used and visualization of the scans was done with Dataviewer and CTVox. Porosity analysis was performed with CTAn by Bruker. The images were binarized and grayscale values were set to 100–255 prior to calculation of the porosity. A FIB-SEM Scios from Thermo Fisher has been used to provide 3D imaging of the pore structure. In order to prepare the sample for the FIB-SEM procedure, the NiMPL-PTL was mechanically cut into a smaller piece of 5 mm × 5 mm for better stability during the high tilt in the tool. Subsequently, the sample was glued on an aluminum sample holder using silver conductive RS glue with the cathode layer facing on top. Slicing of the NiMPL-PTL was done by ion milling using gallium (Ga^+) as the ion source. All cross sections were subsequently made with a focused Ga^+ beam at an accelerating voltage of 30 kV and a current of 15 nA. Each cross-sectional cut

was made at a distance of 100 nm between each section in the z-direction. Consecutive imaging of serial sections was acquired by FEG-SEM at a set magnification of 4,000 × with an additional reduced area focusing on the area of interest. All images were obtained at an acceleration voltage of 20 kV and a current of 1.6 nA. For the sample NiMPL-PTL discussed later, 240 FIB slices were prepared with a milling time of 2 min 34 s and an image processing time of 6 μs per SEM image. Representative FIB-SEM images of the NiMPL-PTL layers before and after slicing are shown in Figure S21. The 240 consecutives SEM images, with a resolution of 34.02 μm (along x) × 39.85 μm (along y) × 24.3 μm (along z) for NiMPL-PTL are then analyzed by different software applications for further information. For preprocessing the SEM images stack, ImageJ was used to filter out the vertical stripes and increase the contrast between the background and target phase. A custom-built MATLAB was used for the image segmentation purpose. The processed images were then imported to Avizo for 3D rendering and estimating the porosity. It is important to note that the FIB-SEM raw pictures are shown in grayscale images in which the darker parts refer to the pores and the brightest ones correspond to the solid matrix. The porosity measurements of the samples have been performed by MIP (Pascal 140/240, Thermo Scientific up to a pressure of 200 MPa). MIP involves forcing mercury into the pores of samples by the application of a pressure to measure the size and volume of pores. As pressure is applied, mercury fills the larger pores first. As pressure increases, the filling proceeds to smaller pores. The pore-size distribution is determined from the volume intruded at each pressure increment. The pore-size distribution is represented as cumulative pore volume and the first derivative of the cumulative curve, $dV/d\log D$ as a function of pore diameter. ICR measurements were performed in order to gain deep information about the electrical resistance behavior with respect to the mechanical compression. The bare PTL and NiMPL-PTL were placed between two Cu cylinders, which were already polished until they have a mirror finish. Carbon papers (Spectracarb 2050A-1050, 10 μm), which were placed between the coating and the Cu surface were used as compressible contact element for the ICR measurements. The sandwich-like configuration was compressed with a hydraulic press, which applied force in the range of 50 to 650 N cm^{-2}. The measurement was performed by applying a direct current of 5 A using a potentiostat (Zahner elektrik IM6) and a booster (Module PP240). The ICRs of the PTLs were determined according to an electrical circuit of resistors connected in series. The ohmic drop resulting from the Cu and carbon paper interface was defined by conducting this experiment using only the carbon paper without any coated specimen. The capillary-pressure curves were calculated using the structure obtained from μ-CT images, implemented in GeoDict. Both local and global pore-size distributions were evaluated using MATLAB functions. The capillary-pressure curves were simulated with GeoDict. The 3D measured structures were imported using the built-in Import-Geo-Vol module. The SatuDict module was used to calculate the capillary-pressure curves for the given structures for imbibition and drainage processes. Wetting and nonwetting phase reservoirs were added in z+ and z- directions, respectively. The boundary conditions were chosen to be symmetric in x and y-directions. The capillary-pressure curves were acquired using a surface tension between water/air of 0.0662 N/m at 60°C and a measured contact angle of 119°. The contact angle changes after cleaning the PTL surface with a mixture of water/ethanol/0.1 M hydrochloric acid from hydrophobic to hydrophilic values, which will slightly increase the measured capillary pressure. From the results of the capillary-pressure curves, the relative gas permeability and diffusivity were calculated. For receiving the geometric tortuosity factor Laplace diffusivity simulations were conducted on both structures using the module DiffuDict. Laplace diffusivity or bulk diffusion considers the diffusing fluid as a continuum. The porosity of the given structure divided by the

resulting effective diffusivity from the simulations gives the tortuosity. The module FlowDict was used to calculate the flow through the structure. PoroDict within GeoDict was used to calculate the pore-size distribution by the granulometry and watershed algorithms (Figure S18). The GeoDict watershed algorithm may give an oversegmentation, so after watershed algorithm a reconnection of fragmented pores was performed by the software. The pore shape was analyzed in addition and is shown in Figure S18B.

AEM electrolyzer test

The catalyst inks were prepared as follows. Ir black or 40% Pt/C as precious metals for anode and cathode, respectively, and Acta 3030 (CuCoOx) and Acta 4030 (Ni/(CeO_2-La_2O_3)/C)) as nonprecious metal catalysts for anode and cathode, respectively, were mixed with 1.5 g of water and 99.95% 2-propanol each. 20 wt % of Sustainion XA-9, 5 wt % in ethanol was added into the catalyst suspension to obtain well-dispersed ink using magnetic stirring combined with ultra-sonication. CCMs were prepared by directly coating the catalysts onto both sides of the membrane (reinforced Sustainion anion exchange membrane x37–50 membranes (50 μm thickness) with an active area 4 cm^2 using hand-spray method with the aid of a spray gun (nitrogen as gas). During the CCM preparation, the dried Sustainion x37 was placed on the vacuum heating plate with an optimal temperature of 60°C, and the catalysts ink was deposited on the membrane. The ionomer and catalyst loading in total was 2.7 mg cm^{-2}. Prior to the testing, CCMs were soaked in a bath of 1 M KOH for 24 h to exchange the chloride ions with hydroxide ions. To minimize the membrane contamination, membrane treatment was done in a closed container to avoid CO_2 contamination (carbonate formation that may affect conductivity). In addition, the 1 M KOH solution was changed several times over this duration to remove any possible solved carbonate out of the solution. Since the Sustainion X37 tends to adsorb the KOH solution immediately leading to curling and wrapping. Therefore, if CCM-based Sustainion membrane is not treated carefully in KOH solution the cell assembly becomes very difficult. Therefore, dried CCM should be placed in a large 1M KOH bath with a soft stretch of the CCM to its corners and then hold the CCM in its corners with some weights during activation. Due to this delicate treating, the resulting treated CCM can preserve a memory of flattening state and remain completely flat during the cell assemblies. Finally, the obtained membranes were rinsed thoroughly with deionized water before further use. The CCMs after preparation were placed between 4 cm^2 piece of carbon paper (Spectracarb 2050A-1050) and Ni felt from the cathode and anode side, respectively, prior to being sandwiched between PTLs. Carbon paper and nickel felt are used to allow applying enough force while clamping the cell and consequently to avoid harming a sensitive activated membrane. A CCM with carbon paper and nickel felt on both sides is considered to be the MEA. These MEAs were finally mechanically placed between two PTLs, which were immersed in mixture of ethanol/water/0.5 M hydrochloric acid for 3 min, when assembling the cell hardware to remove the possible oxide layer on the surface before cell assembly. Bipolar plates are mounted at both sides of the PTLs and the cell was assembled using four tie rods with a clamping force of 130 N cm^{-2} as it is schematized in Figures 4A, 4B, S7A, and S7B, four different cells with different configurations are fabricated by directly placing the MEAs between different APS coated and uncoated PTL: (1) two uncoated PTLs for both anode and cathode sides (PTL/PTL), (2) uncoated PTL for the cathode side and NiMPL-PTL for the anode side (PTL/NiMPL-PTL), (3) NiMPL-PTL for the cathode side and uncoated PTL for the anode side (NiMPL-PTL/PTL), and (4) two NiMPL-PTL for anode and cathode side (NiMPL-PTL/NiMPL-PTL). For comparison, one cell was also fabricated using commercial Ni meshes as PTL.

Cell performance evaluation

The electrochemical performance was measured in an in-house-produced AEM water electrolyzer in pure water at 60°C. After 30 min of activation at constant current density of 0.2 A cm^{-2}, the cells were characterized by recording polarization curves up to 0.5 A cm^2 with the scan rate of 10 mV/s. EIS was performed at different current densities by using a potentiostat/galvanostat (Biologic VSP-300) and 10A booster and plotted from 50 kHz to 100 mHz. The operating conditions and cell hardware were kept the same for all MEAs. To analyze the EIS plots, fitting procedure was with the equivalent circuit chosen based on the physical processes and their interactions in our system, which include ohmic, activation, and mass-transfer resistance. EIS was applied to identify the ohmic, activation and mass-transfer losses. In case of the test performed with precious metal-based catalysts, the equivalent circuit includes two CPE pairs from high to low frequency range as two semicircle loops are observed in the Nyquist plots from Figure 4D. For nonprecious metal-based catalysts the equivalent circuit includes three CPE pairs from high to low frequency range as two semicircle loops are observed in the Nyquist plots from Figure 5B. The fitting of Nyquist plot is done by RelaxIS software. Impedance data for nonprecious metal-based MEA PTL/PTL shows very small low-frequency inductive loops, which is reported to be due to the membrane degradation and membrane thinning.[78] This distorted low-frequency inductive loops from the Nyquist plot observed at low frequencies is too small to be fitted. Using RelaxIS software, for the Nyquist plot fitting, the effect of high-frequency tail extending toward positive imaginary parts, which is considered to be due to the electronics and wires is included.

SUPPLEMENTAL INFORMATION

Supplemental information can be found online at https://doi.org/10.1016/j.joule.2021.05.006.

ACKNOWLEDGMENTS

The authors thank Dr. Noriko Sata (DLR Stuttgart) for her support on XRD and MIP analysis, Ina Plock (DLR Stuttgart) for her support on SEM analysis, Mr. Volker Thielke (DLR Stuttgart) for his support on plasma spraying, Mr. Günter Roth (DLR Stuttgart) for his support on metallographic analysis, and Mr. Jörg Bürkle (DLR Stuttgart) for his assistance during experimental works.

AUTHOR CONTRIBUTIONS

F.R. designed the experiments and carried out the electrochemical test along with analysis of electrochemical and physical results and writing of the manuscript. T.M. conducted the numerical simulation and contributed to writing of the simulation part and editing the manuscript. E.T. analyzed the FIB-SEM images by different software applications and edited the manuscript. E.H. carried out the FIB-SEM characterization and edited the manuscript. L.M. carried out the μ-CT characterization and analyzed the data and also edited the manuscript. M.G. carried out the analysis and fitting of the impedance data and edited the manuscript. B.D.W. provided helpful suggestions and edited the manuscript. C.H. provided and supported the work with the device and the software for analyzing the μ-CT characterization, provided helpful suggestions, and edited the manuscript. A.S.G. provided helpful suggestions and support during the manuscript preparation and edited the manuscript. S.A.A. designed and formulated the NiMPL-PTL and provided support on each stage of various tests and manuscript preparation. K.A.F. provided helpful suggestions and support during the manuscript preparation and edited the manuscript. All authors discussed the results and commented on the manuscript.

DECLARATION OF INTERESTS

The authors declare no competing interests.

Received: January 22, 2021
Revised: April 29, 2021
Accepted: May 7, 2021
Published: June 9, 2021

REFERENCES

1. Yan, Z., Hitt, J.L., Turner, J.A., and Mallouk, T.E. (2020). Renewable electricity storage using electrolysis. Proc. Natl. Acad. Sci. USA *117*, 12558–12563.

2. Kojima, H., Matsuda, T., Matsumoto, H., and Tsujimura, T. (2018). Development of dynamic simulator of alkaline water electrolyzer for optimizing renewable energy systems. J. Int. Counc. Electr. Eng. *8*, 19–24.

3. Esposito, D.V. (2017). Membraneless electrolyzers for low-cost hydrogen production in a renewable energy future. Joule *1*, 651–658.

4. Lavorante, M.J., Reynoso, C.Y., and Franco, J.I. (2015). Water electrolysis with zirfon as separator and NaOH as electrolyte. Desalin. Water Treat. *56*, 3647–3653.

5. Zeng, K., and Zhang, D. (2010). Recent progress in alkaline water electrolysis for hydrogen production and applications. Prog. Energy Combust. Sci. *36*, 307–326.

6. Bender, G., Carmo, M., Smolinka, T., Gago, A., Danilovic, N., Mueller, M., Ganci, F., Fallisch, A., Lettenmeier, P., Friedrich, K.A., et al. (2019). Initial approaches in benchmarking and round robin testing for proton exchange membrane water electrolyzers. Int. J. Hydr. Energy *44*, 9174–9187.

7. Grigoriev, S.A., Millet, P., Korobtsev, S.V., Porembskiy, V.I., Pepic, M., Etievant, C., Puyenchet, C., and Fateev, V.N. (2009). Hydrogen safety aspects related to high-pressure polymer electrolyte membrane water electrolysis. Int. J. Hydr. Energy *34*, 5986–5991.

8. Bernt, M., Hartig-Weiß, A., Tovini, M.F., El-Sayed, H.A., Schramm, C., Schröter, J., Gebauer, C., and Gasteiger, H.A. (2020). Current challenges in catalyst development for PEM water electrolyzers. Chem. Ing. Tech. *92*, 31–39.

9. Kraglund, M.R., Carmo, M., Schiller, G., Ansar, S.A., Aili, D., Christensen, E., and Jensen, J.O. (2019). Ion-solvating membranes as a new approach towards high rate alkaline electrolyzers. Energy Environ. Sci. *12*, 3313–3318.

10. Zlobinski, M., Schuler, T., Büchi, F.N., Schmidt, T.J., and Boillat, P. (2020). Transient and steady state two-phase flow in anodic porous transport layer of proton exchange membrane water electrolyzer. J. Electrochem. Soc. *167*, 084509.

11. Guo, Q., Ye, F., Guo, H., and Ma, C.F. (2017). Gas/water and heat management of PEM-based fuel cell and electrolyzer systems for space applications. Microgravity Sci. Technol. *29*, 49–63.

12. Suermann, M., Gimpel, T., Bühre, L.V., Schade, W., Bensmann, B., and Hanke-Rauschenbach, R. (2020). Femtosecond laser-induced surface structuring of the porous transport layers in proton exchange membrane water electrolysis. J. Mater. Chem. A *8*, 4898–4910.

13. Leonard, E., Shum, A.D., Danilovic, N., Capuano, C., Ayers, K.E., Pant, L.M., Weber, A.Z., Xiao, X., Parkinson, D.Y., and Zenyuk, I.V. (2020). Interfacial analysis of a PEM electrolyzer using X-ray computed tomography. Sustainable Energy Fuels *4*, 921–931.

14. Razmjooei, F., Farooqui, A., Reissner, R., Gago, A.S., Ansar, S.A., and Friedrich, K.A. (2020). Elucidating the performance limitations of alkaline electrolyte membrane electrolysis: dominance of anion concentration in membrane electrode assembly. ChemElectroChem *7*, 3951–3960.

15. Kumar, S.S., and Himabindu, V. (2019). Hydrogen production by PEM water electrolysis- a Review. Mater. Sci. Energy Technol. *2*, 442–454.

16. Grigoriev, S.A., Porembsky, V.I., and Fateev, V.N. (2006). Pure hydrogen production by PEM electrolysis for hydrogen energy. Int. J. Hydr. Energy *31*, 171–175.

17. Song, S., Zhang, H., Ma, X., Shao, Z., Baker, R.T., and Yi, B. (2008). Electrochemical investigation of electrocatalysts for the oxygen evolution reaction in PEM water electrolyzers. Int. J. Hydr. Energy *33*, 4955–4961.

18. Rakousky, C., Reimer, U., Wippermann, K., Carmo, M., Lueke, W., and Stolten, D. (2016). An analysis of degradation phenomena in polymer electrolyte membrane water electrolysis. J. Power Sources *326*, 120–128.

19. Sun, S., Shao, Z., Yu, H., Li, G., and Yi, B. (2014). Investigations on degradation of the long-term proton exchange membrane water electrolysis stack. J. Power Sources *267*, 515–520.

20. Aricò, A.S., Siracusano, S., Briguglio, N., Baglio, V., Di Blasi, A., and Antonucci, V. (2013). Polymer electrolyte membrane water electrolysis: status of technologies and potential applications in combination with renewable power sources. J. Appl. Electrochem. *43*, 107–118.

21. Schuler, T., Ciccone, J.M., Krentscher, B., Marone, F., Peter, C., Schmidt, T.J., and Büchi, F.N. (2020). Hierarchically structured porous transport layers for polymer electrolyte water electrolysis. Adv. Energy Mater. *10*, 1903216.

22. Lettenmeier, P., Kolb, S., Sata, N., Fallisch, A., Zielke, L., Thiele, S., Gago, A.S., and Friedrich, K.A. (2017). Comprehensive investigation of novel pore-graded gas diffusion layers for high-performance and cost-effective proton exchange membrane electrolyzers. Energy Environ. Sci. *10*, 2521–2533.

23. Santos, D.M.F., Sequeira, C.A.C., and Figueiredo, J.L. (2013). Hydrogen production by alkaline water electrolysis. Quim. Nova *36*, 1176–1193.

24. Razmjooei, F., Singh, K.P., Yang, D.-S., Cui, W., Jang, Y.H., and Yu, J.-S. (2017). Fe-treated heteroatom (S/N/B/P)-doped graphene electrocatalysts for water oxidation. ACS Catal *7*, 2381–2391.

25. Singh, K.P., Shin, C.-H., Lee, H.-Y., Razmjooei, F., Sinhamahapatra, A., Kang, J., and Yu, J.-S. (2020). TiO_2/ZrO_2 nanoparticle composites for electrochemical hydrogen evolution. ACS Appl. Nano Mater. *3*, 3634–3645.

26. Xu, Q., Oener, S.Z., Lindquist, G., Jiang, H., Li, C., and Boettcher, S.W. (2021). Integrated reference electrodes in anion-exchange-membrane electrolyzers: impact of stainless-steel gas-diffusion layers and internal mechanical pressure stainless-steel gas-diffusion layers and internal mechanical pressure. ACS Energy Lett *6*, 305–312.

27. Huang, G., Mandal, M., Hassan, N.U., Groenhout, K., Dobbs, A., Mustain, W.E., and Kohl, P.A. (2020). Ionomer optimization for water uptake and swelling in anion exchange membrane electrolyzer: oxygen evolution electrode. J. Electrochem. Soc. *167*, 164514.

28. Parrondo, J., Arges, C.G., Niedzwiecki, M., Anderson, E.B., Ayers, K.E., and Ramani, V. (2014). Degradation of anion exchange membranes used for hydrogen production by UltraPure water electrolysis. RSC Adv *4*, 9875–9879.

29. Pandiarajan, T., John Berchmans, L.J., and Ravichandran, S. (2015). Fabrication of spinel ferrite based alkaline anion exchange membrane water electrolysers for hydrogen production. RSC Adv *5*, 34100–34108.

30. Seetharaman, S., Balaji, R., Ramya, K., Dhathathreyan, K.S., and Velan, M. (2013). Graphene oxide modified non-noble metal electrode for alkaline anion exchange membrane water electrolyzers. Int. J. Hydr. Energy *38*, 14934–14942.

31. Pavel, C.C., Cecconi, F., Emiliani, C., Santiccioli, S., Scaffidi, A., Catanorchi, S., and Comotti, M. (2014). Highly efficient platinum group metal free based membrane-electrode assembly for anion exchange membrane water electrolysis. Angew. Chem. Int. Ed. Engl. *53*, 1378–1381.

32. Leng, Y., Chen, G., Mendoza, A.J., Tighe, T.B., Hickner, M.A., and Wang, C.Y. (2012). Solid-state water electrolysis with an alkaline membrane. J. Am. Chem. Soc. *134*, 9054–9057.

33. Xiao, L., Zhang, S., Pan, J., Yang, C., He, M., Zhuang, L., and Lu, J. (2012). First implementation of alkaline polymer electrolyte water electrolysis working only with pure water. Energy Environ. Sci. *5*, 7869–7871.

34. Ganesan, P., Sivanantham, A., and Shanmugam, S. (2018). CoS_2–TiO_2 hybrid nanostructures: efficient and durable bifunctional electrocatalysts for alkaline electrolyte membrane water electrolyzers. J. Mater. Chem. A *6*, 1075–1085.

35. Ganesan, P., Sivanantham, A., and Shanmugam, S. (2016). Inexpensive electrochemical synthesis of nickel iron sulphides on nickel foam: super active and ultra-durable electrocatalysts for alkaline electrolyte membrane water electrolysis. J. Mater. Chem. A *4*, 16394–16402.

36. Wang, L., Weissbach, T., Reissner, R., Ansar, A., Gago, A.S., Holdcroft, S., and Friedrich, K.A. (2019). High performance anion exchange membrane electrolysis using plasma-sprayed, non-precious-metal electrodes. ACS Appl. Energy Mater. *2*, 7903–7912.

37. Vincent, I., and Bessarabov, D. (2018). Low cost hydrogen production by anion exchange membrane electrolysis: a review. Renew. Sustain. Energy Rev. *81*, 1690–1704.

38. Cho, M.K., Lim, A., Lee, S.Y., Kim, H.-J., Yoo, S.J., Sung, Y.-E., Park, H.S., and Jang, J.H. (2017). A Review on membranes and catalysts for anion exchange membrane water electrolysis single cells. J. Electrochem. Sci. Technol. *8*, 183–196.

39. Henkensmeier, D., Najibah, M., Harms, C., Žitka, Y., Hnát, Y., and Bouzek, K. (2021). Overview: state-of-the art commercial membranes for anion exchange membrane water electrolysis. J. Electrochem. Conv. Stor. *18*, 024001.

40. Wei, J., Zhou, M., Long, A., Xue, Y., Liao, H., Wei, C., and Xu, Z.J. (2018). Heterostructured electrocatalysts for hydrogen evolution reaction under alkaline conditions. Nanomicro. Lett. *10*, 75.

41. Frensch, S.H., Olesen, A.C., Araya, S.S., and Kær, S.K. (2018). Model-supported characterization of a PEM water electrolysis cell for the effect of compression. Electrochim. Acta *263*, 228–236.

42. Stähler, M., Stähler, A., Scheepers, F., Carmo, M., Lehnert, W., and Stolten, D. (2020). Impact of porous transport layer compression on hydrogen permeation in PEM water electrolysis. Int. J. Hydr. Energy *45*, 4008–4014.

43. Mo, J., Kang, Z., Yang, G., Retterer, S.T., Cullen, D.A., Toops, T.J., Green, J.B., Jr., and Zhang, F.-Y. (2016). Thin liquid/gas diffusion layers for high-efficiency hydrogen production from water splitting. Appl. Energy *177*, 817–822.

44. Grigoriev, S.A., Millet, P., Volobuev, S.A., and Fateev, V.N. (2009). Optimization of porous current collectors for PEM water electrolysers. Int. J. Hydr. Energy *34*, 4968–4973.

45. Mo, J., Kang, Z., Retterer, S.T., Cullen, D.A., Toops, T.J., Green, J.B., Jr., Mench, M.M., and Zhang, F.Y. (2016). Discovery of true electrochemical reactions for ultrahigh catalyst mass activity in water splitting. Sci. Adv. *2*, e1600690.

46. Majasan, J.O., Iacoviello, F., Shearing, P.R., and Brett, D.J. (2018). Effect of microstructure of porous transport layer on performance in polymer electrolyte membrane water electrolyser. Energy Procedia *151*, 111–119.

47. Lopata, J., Kang, Z., Young, J., Bender, G., Weidner, J.W., and Shimpalee, S. (2020). Effects of the transport/catalyst layer interface and catalyst loading on mass and charge transport phenomena in polymer electrolyte membrane water electrolysis devices. J. Electrochem. Soc. *167*, 064507.

48. Hackemüller, F.J., Borgardt, E., Panchenko, O., Müller, M., and Bram, M. (2019). Manufacturing of large-scale titanium-based porous transport layers for polymer electrolyte membrane electrolysis by tape casting. Adv. Eng. Mater. *21*, 1801201.

49. Liu, C., Carmo, M., Bender, G., Everwand, A., Lickert, T., Young, J.L., Smolinka, T., Stolten, D., and Lehnert, W. (2018). Performance enhancement of PEM electrolyzers through iridium-coated titanium porous transport layers. Electrochem. Commun. *97*, 96–99.

50. Lee, C.H., Lee, J.K., Zhao, B., Fahy, K.F., LaManna, J.M., Baltic, E., Hussey, D.S., Jacobson, D.L., Schulz, V.P., and Bazylak, A. (2020). Temperature-dependent gas accumulation in polymer electrolyte membrane electrolyzer porous transport layers. J. Power Sources *446*, 227312.

51. Mandal, M. (2021). Recent advancement on anion exchange membranes for fuel cell and water electrolysis. ChemElectroChem *8*, 36–45.

52. Miller, H.A., Bouzek, K., Hnat, J., Loos, S., Bernäcker, C.I., Weißgärber, T., Röntzsch, L., and Meier-Haack, J. (2020). Green hydrogen from anion exchange membrane water electrolysis: a review of recent developments in critical materials and operating conditions. Sustainable Energy Fuels *4*, 2114–2133.

53. Gago, A.S., Ansar, S.A., Saruhan, B., Schulz, U., Lettenmeier, P., Cañas, N.A., Gazdzicki, P., Morawietz, T., Hiesgen, R., Arnold, J., and Friedrich, K.A. (2016). Protective coatings on stainless steel bipolar plates for proton exchange membrane (PEM) electrolysers. J. Power Sources *307*, 815–825.

54. Razmjooei, F., Liu, T., Azevedo, D.A., Hadjixenophontos, E., Reissner, R., Schiller, G., Ansar, S.A., and Friedrich, K.A. (2020). Improving plasma sprayed Raney-type nickel-molybdenum electrodes towards high-performance hydrogen evolution in alkaline medium. Sci. Rep. *10*, 10948.

55. Wittmann-Ténèze, K., Caron, N., and Alexandre, S. (2008). Gas permeability of porous plasma-sprayed coatings. J. Therm. Spray Tech. *17*, 902–907.

56. Cipitria, A., Golosnoy, I.O., and Clyne, T.W. (2007). Sintering kinetics of plasma-sprayed zirconia TBCs. J. Therm. Spray Tech. *16*, 809–815.

57. Odhiambo, J.G., Li, W.G., Zhao, Y.T., and Li, C.L. (2019). Porosity and its significance in plasma-sprayed coatings. Coatings *9*, 460–479.

58. Tillmann, W., Khalil, O., and Abdulgader, M. (2019). Porosity characterization and its effect on thermal properties of APS-sprayed alumina coatings. Coatings *9*, 601.

59. Altaf, H., Vorhauer, N., Tsotsas, E., and Vidaković-Koch, T. (2020). Steady-state water drainage by oxygen in anodic porous transport layer of electrolyzers: a 2D pore network study. Processes *8*, 362.

60. Lettenmeier, P., Wang, R., Abouatallah, R., Saruhan, B., Freitag, O., Gazdzicki, P., Morawietz, T., Hiesgen, R., Gago, A.S., and Friedrich, K.A. (2017). Low-cost and durable bipolar plates for proton exchange membrane electrolyzers. Sci. Rep. *7*, 44035.

61. Rodríguez, J., Palmas, S., Sánchez-Molina, M., Amores, E., Mais, L., and Campana, R. (2019). Simple and precise approach for determination of ohmic contribution of diaphragms in alkaline water electrolysis. Membranes *9*, 129.

62. Siracusano, S., Trocino, S., Briguglio, N., Baglio, V., and Aricò, A.S. (2018). Electrochemical impedance spectroscopy as a diagnostic tool in polymer electrolyte membrane electrolysis. Materials (Basel) *11*, 1368.

63. Li, D., Park, E.J., Zhu, W., Shi, Q., Zhou, Y., Tian, H., Lin, Y., Serov, A., Zulevi, B., Baca, E.D., et al. (2020). Highly quaternized polystyrene ionomers for high performance anion exchange membrane water electrolysers. Nat. Energy *5*, 378–385.

64. Millet, P., Ranjbari, A., de Guglielmo, F., Grigoriev, S.A., and Auprêtre, F. (2012). Cell failure mechanisms in PEM water electrolyzers. Int. J. Hydr. Energy *37*, 17478–17487.

65. Minnaar, C., De Beer, F.D., and Bessarabov, D. (2020). Current density distribution of electrolyzer flow fields: in situ current mapping and neutron radiography. Energy Fuels *34*, 1014–1023.

66. Zheng, Y., Jiao, Y., Vasileff, A., and Qiao, S.Z. (2018). The hydrogen evolution reaction in alkaline solution: from theory, single crystal models, to practical electrocatalysts. Angew. Chem. Int. Ed. Engl. *57*, 7568–7579.

67. Faid, A.Y., Oyarce Barnett, A.O., Seland, F., and Sunde, S. (2018). Highly active nickel-based catalyst for hydrogen evolution in anion exchange membrane electrolysis. Catalysts *8*, 614.

68. Oener, S.Z., Foster, M.J., and Boettcher, S.W. (2020). Accelerating water dissociation in bipolar membranes and for electrocatalysis. Science *369*, 1099–1103.

69. Ito, H., Kawaguchi, N., Someya, S., Munakata, T., Miyazaki, N., Ishida, M., and Nakano, A. (2018). Experimental investigation of electrolytic solution for anion exchange membrane water electrolysis. Int. J. Hydr. Energy *43*, 17030–17039.

70. Kong, C.S., Kim, D.-Y., Lee, H.-K., Shul, Y.-G., and Lee, T.-H. (2002). Influence of pore-size distribution of diffusion layer on mass-transport

problems of proton exchange membrane fuel cells. J. Power Sources *108*, 185–191.

71. Dong, D., Shao, X., Hu, X., Chen, K., Xie, K., Yu, L., Ye, Z., Yang, P., Parkinson, G., and Li, C.-Z. (2016). Improved gas diffusion within microchanneled cathode supports of SOECs for steam electrolysis. Int. J. Hydr. Energy *41*, 19829–19835.

72. Li, Y., Kang, Z., Deng, X., Yang, G., Yu, S., Mo, J., Talley, D.A., Jennings, G.K., and Zhang, F.-Y. (2019). Wettability effects of thin titanium liquid/gas diffusion layers in proton exchange membrane electrolyzer cells. Electrochim. Acta *298*, 704–708.

73. Lee, J.K., Lee, C.H., and Bazylak, A. (2019). Pore network modelling to enhance liquid water transport through porous transport layers for polymer electrolyte membrane electrolyzers. J. Power Sources *437*, 226910.

74. Lee, J.K., Lee, C.H., Fahy, K.F., Kim, P.J., Krause, K., LaManna, J.M., Baltic, E., Jacobson, D.L., Hussey, D.S., and Bazylak, A. (2020). Accelerating bubble detachment in porous transport layers with patterned through-pores. ACS Appl. Energy Mater. *3*, 9676–9684.

75. Kadyk, T., Bruce, D., and Eikerling, M. (2016). How to enhance gas removal from porous electrodes? Sci. Rep. *6*, 38780.

76. Epstein, N. (1989). On tortuosity and the tortuosity factor in flow and diffusion through porous media. Chem. Eng. Sci. *44*, 777–779.

77. Schuler, T., De Bruycker, R.D., Schmidt, T.J., and Büchi, F.N. (2019). Polymer electrolyte water electrolysis: correlating porous transport layer structural properties and performance: part I. tomographic analysis of morphology and topology. J. Electrochem. Soc. *166*, F270–F281.

78. Vincent, I., Lee, E.C., and Kim, H.M. (2021). Comprehensive impedance investigation of low-cost anion exchange membrane electrolysis for large-scale hydrogen production. Sci. Rep. *11*, 293.